Structural, Optical, and Photoelectrochemical Properties of Nanocrystalline TiO 2 –In 2 O 3 Composite Solids and Films Prepared by Sol–Gel Method

ARTICLE *in* THE JOURNAL OF PHYSICAL CHEMISTRY B · MAY 2001

Impact Factor: 3.3 · DOI: 10.1021/jp003247r

3 AUTHORS:

S.K. Poznyak
Belarusian State University
71 PUBLICATIONS **1,759** CITATIONS
SEE PROFILE

Dmitri V Talapin
University of Chicago
160 PUBLICATIONS **16,259** CITATIONS
SEE PROFILE

Anatoly Kulak
Institute of General and Inorganic Chemistry,…
113 PUBLICATIONS **971** CITATIONS
SEE PROFILE

Structural, Optical, and Photoelectrochemical Properties of Nanocrystalline $TiO_2-In_2O_3$ Composite Solids and Films Prepared by Sol−Gel Method

Sergey K. Poznyak,*,† Dmitri V. Talapin,†,§ and Anatoly I. Kulak‡

Institute of Physico-Chemical Problems, Belarusian State University, Leningradskaya St. 14, Minsk 220050, Belarus, and Institute of General and Inorganic Chemistry, Belarusian Academy of Sciences, Surganova St. 9, Minsk 220072, Belarus

Received: September 13, 2000; In Final Form: February 21, 2001

Nanocrystalline titanium and indium oxides and $TiO_2-In_2O_3$ composites have been prepared by sol−gel technique using concentrated hydrous titanium dioxide and indium hydroxide sols. Structure, optical, and photoelectrochemical properties of the composites with different molar ratios of TiO_2 to In_2O_3 have been studied. The binary oxide films and xerogels annealed at temperatures from 200 to 700 °C have a nanocrystalline structure without the chemical interaction between the oxides. However, there is a strong mutual influence of the components of the binary oxide systems, during their annealing which manifests itself in thermogravimetry and differential scanning calorimetry measurements and in a marked effect on the oxide crystallite size. Highly transparent $TiO_2-In_2O_3$ films fabricated by spin-coating technique exhibit extreme dependencies of the various optical and photoelectrochemical properties on the film composition. The band gap edge of the composite films is blue-shifted, as compared with that of single-component films. Possible causes of these effects have been discussed. The conductivity of $TiO_2-In_2O_3$ films changes by 6 orders of magnitude in the range of compositions near the calculated value for percolation threshold associated with the formation of 3D infinite clusters of interconnected In_2O_3 nanoparticles.

1. Introduction

Significant interest has been generated during the past decade in the field of preparing nanostructured oxides for various applications. Fabrication of nanoscaled heterogeneous composites offers additional possibilities in developing novel materials. There are a lot of reports on sol−gel-derived nanocomposite films and powders based on the binary oxides such as TiO_2-SiO_2,[1−4] $Al_2O_3-SiO_2$,[5] TiO_2-WO_3,[6,7] TiO_2-CeO_2,[8] $TiO_2-Fe_2O_3$,[9] $In_2O_3-MoO_3$,[10] and others, which have been considered as promising antireflecting windows,[1] electrochromic materials,[6,8,9] catalysts,[2,3,5] photocatalysts,[3] and sensor elements.[10] It has been shown that properties of composites obtained often cannot be considered as a simple superposition of the properties of individual components due to strong surface interactions between the closely packed nanoparticles in the binary oxide systems.[2−5,7]

Titanium dioxide is widely used material in producing pigments,[11] catalysts,[12] photocatalysts,[13,14] solar cells,[15] optical thin film filters,[16] etc. The optical and electrical properties of doped In_2O_3 films make them very well suited as transparent conducting window coatings.[17,18] Moreover, indium oxide has been shown to be promising material for gas sensors.[19,20] Sol−gel-derived nanostructured TiO_2 and In_2O_3 films have been prepared, and different properties of them have been studied by a number of researchers.[20−24] However, to our knowledge, $TiO_2-In_2O_3$ mixed nanocrystalline materials have not been investigated.

One of the convenient methods of nanocomposite preparation is a coprecipitation of the oxides from a solution containing inorganic salts or alkoxides of metals. An important problem associated with this method is the unequal hydrolysis rates of the precursors, which may result in the segregation of one-component-rich phases during the synthesis.[3] This problem may be successfully overcome when employing preliminarily prepared stabilized sols of individual oxide components which are mixed in an appropriate proportion before obtaining a composite material. In addition, sol products have frequently properties ideal for thin-film deposition, which is useful for materials processing.[25] Reports on the synthesis and characterization of nanocomposite materials prepared by sol−gel method have been recently reviewed.[26]

In the present work, highly transparent $TiO_2-In_2O_3$ composite films were fabricated from stabilized TiO_2 and $In(OH)_3$ sols preliminarily prepared using inorganic precursors. Structural transformations in the binary oxide samples with various Ti/In ratio during the thermal treatment and the crystallinity of the composites were studied by thermogravimetric analysis (TGA), differential scanning calorimetry (DSC), and X-ray diffraction method (XRD). The optical and photoelectrochemical (PEC) properties of the composite films were examined and discussed.

2. Experimental Section

2.1. Materials Synthesis. All chemicals used were of analytical grade or of the highest purity available. $TiCl_4$ was purified by distillation. The solutions were prepared using doubly distilled water.

$TiO_2-In_2O_3$ nanocrystalline xerogels and films were fabricated from stabilized hydrous titanium dioxide and indium

* Corresponding author. E-mail: elchem@fhp.bsu.unibel.by. Fax: +375 172 264696.

† Institute of Physico-Chemical Problems.

‡ Institute of General and Inorganic Chemistry.

§ Present address: Institut für Physikalische Chemie, Universität Hamburg, 20146 Hamburg, Germany.

10.1021/jp003247r CCC: $20.00
Published on Web 05/09/2001

hydroxide sols mixed in a definite proportion. Through this paper, mixed oxide samples are designed by the molar ratio of TiO_2 to In_2O_3, e.g., $TiO_2(0.91)-In_2O_3(0.09)$. Titanium dioxide sol was prepared by the following method. A 15 mL sample of $TiCl_4$ cooled to −20 °C was added dropwise to 53 mL of 0.65 M aqueous HCl solution (0 °C) under vigorous stirring in ice−water bath. The transparent solution obtained was titrated slowly by a 12% aqueous solution of NH_4OH under continuous stirring at 0 °C. Titration was carried out up to a final pH of about 5. The precipitate was washed thoroughly with distilled water until the concentration of chloride in the washings was below 10^{-5} M. After 0.8 mL of concentrated HNO_3 was added as a stabilizer, the precipitate was ultrasonically treated to obtain a transparent TiO_2 sol (ca. 80 g/L) stable for several months at room temperature. Indium hydroxide sol was prepared by an analogous fashion using 0.25 M indium nitrate solution as a starting material.

Thin films were deposited onto quartz substrates for optical measurements and onto conducting F-doped SnO_2 films on a glass sheet for PEC measurements by spin coating process and then heated at 200 °C for 20 min. This procedure was repeated several times to achieve the required film thickness. Finally, the samples were fired at different temperatures ranging from 200 to 700 °C for 1 h in air. The film thickness estimated using transmission electron microscopy data was 0.12−0.15 μm after four deposition cycles.

2.2. Apparatus and Chemicals. Thermogravimetric analysis (TGA) and differential scanning calorimetry analysis (DSC) were carried out using a Metler 3000 thermal analysis system under air atmosphere. The programmed heating rate was 5 °C/min. X-ray diffraction analysis of the films was performed on a HZG 4A powder diffractometer (Carl Zeiss, Jena) using CoK_α radiation (Mn filter). The average crystallite size was estimated from the X-ray line broadening according to Scherrer's equation. Optical transmission, absorption, and specular reflection spectra of the films were measured using Cary 500 UV−vis−NIR spectrometer (Varian). The refractive indexes were calculated from the specular reflection data for the p-component of monochromatic light incident on the film at variable angles.[27]

Photoelectrochemical measurements were carried out in a standard three-electrode cell equipped with an optical quality quartz window. A platinum counter-electrode and an Ag|AgCl|-KCl (sat.) electrode as the reference electrode (+0.201 V vs SHE) were used in this cell. All potentials were determined with respect to this reference electrode and controlled by a conventional potentiostat with a programmer. Photocurrent spectra were obtained using a setup equipped with a high-intensity grating monochromator, a 1000-W xenon lamp, and a slowly rotating light chopper (0.3 Hz). The system was calibrated using an optical power meter, and spectral dependences of the photocurrent were corrected for the spectral intensity distribution at the monochromator output. The photoelectrochemical measurements were made at room temperature in 0.1 M NaOH + 0.1 M CH_3COONa solution.

For conductivity measurements, the films with different TiO_2 to In_2O_3 molar ratios were deposited onto quartz substrates with a pair of comb-shaped Cr/Au electrodes formed by electron beam evaporation (electrode spacing was 100 μm). The conductivity of the films was found to be strongly influenced by some environmental factors such as humidity and exposure to the scattered visible light. Therefore, the resistance of the samples was measured after long-term standing in a closed vessel containing phosphorus (V) oxide as a drying agent.

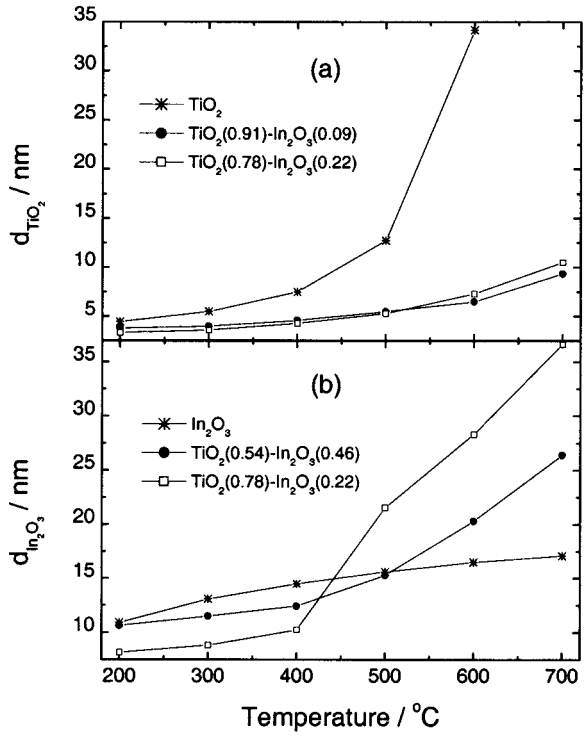

Figure 1. Average size of anatase (a) and In_2O_3 (b) crystallites as a function of the annealing temperature for xerogels with different composition.

3. Results and Discussion

3.1. X-Ray Diffraction Studies. XRD analysis of xerogels obtained by drying the pure TiO_2 sol at 70 °C shows the presence of the nanocrystalline anatase phase. The thermal treatment of this xerogel results in the growth of anatase crystallites, and the anatase-to-rutile transformation begins to occur at 450−500 °C. This process is practically completed at 700 °C, and only the rutile phase takes place at $T > 700$ °C. The pure indium hydroxide xerogel dried at 70 °C is almost amorphous, with some amount of the cubic $In(OH)_3$ phase. According to XRD data, this xerogel heated at $T \geq 200$ °C consists of only the cubic In_2O_3 phase.

X-ray diffraction study of the $TiO_2-In_2O_3$ composites annealed at different temperatures up to 800 °C does not reveal any other phase except those observed in the individual xerogels. This result evidences that the chemical interaction of TiO_2 with In_2O_3 does not occur in the mentioned temperature range. This observation accords with the results reported by Rozdin et al.,[28] who have shown that the co-deposited titanium and indium hydroxides interact to form indium titanate In_2TiO_5 only at temperatures above 850 °C. It should be noted that in the composite samples, the anatase-to-rutile transformation takes place at markedly higher temperatures than that in the pure TiO_2 xerogel. Therefore, for the $TiO_2(0.91)-In_2O_3(0.09)$ composition, traces of the rutile phase appear only at 700 °C.

Figure 1 shows the dependencies of the average crystallite size of anatase and cubic In_2O_3, estimated from the XRD peaks' half-width, on the annealing temperature for xerogels with different composition. In the case of the pure oxide xerogels, crystallites grow from 4.5 to 34 nm for TiO_2 and from 11 to 16.5 nm for In_2O_3 as the annealing temperature increases from 200 to 600 °C (Figure 1). In the binary oxide xerogels, the anatase crystallite growth is markedly suppressed during the thermal treatment. Therefore, for the $TiO_2(0.91)-In_2O_3(0.09)$ composite heated at 600 °C, the average diameter of anatase

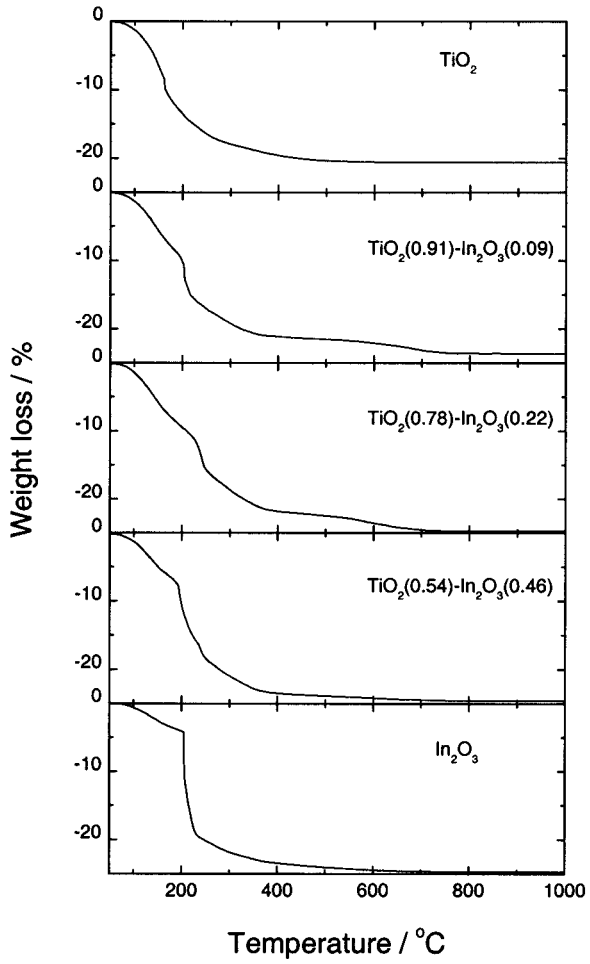

Figure 2. TG curves for single-component hydrous titanium dioxide and indium hydroxide xerogels as well as for $TiO_2-In_2O_3$ binary oxide systems obtained by drying the corresponding sols at 70 °C.

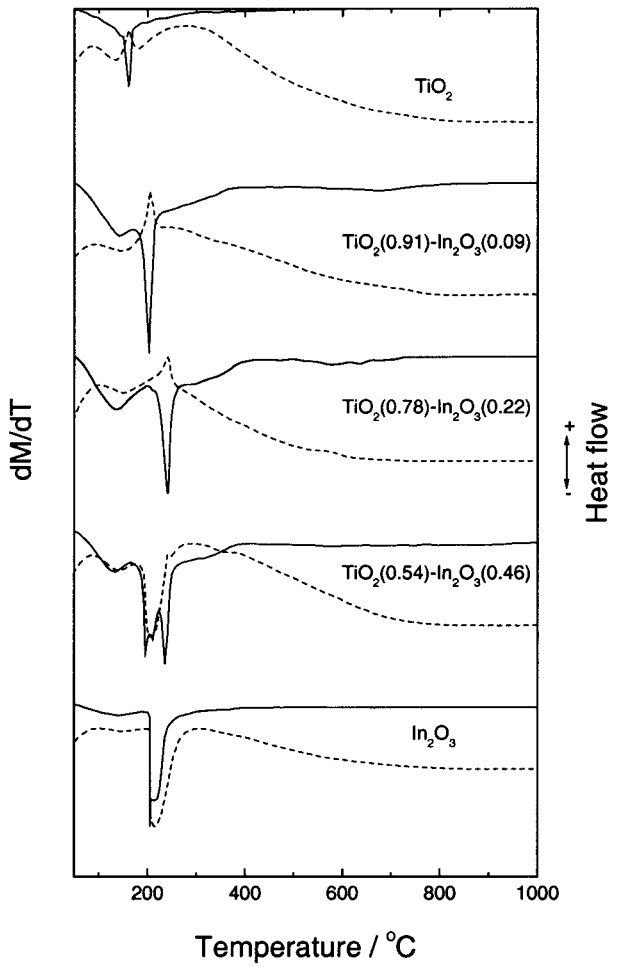

Figure 3. DTG (—) and DSC (– – –) curves for TiO_2, In_2O_3, and $TiO_2-In_2O_3$ composite xerogels obtained by drying the corresponding sols at 70 °C.

crystallites does not exceed 7 nm. A similar effect of retarding the crystallization process has been previously observed for other different co-deposited metal oxides and hydroxides and has come to be known as "mutual protective action against crystallization".[29]

The trend in changing the size of In_2O_3 crystallites in the binary oxide systems during the thermal treatment is more unusual. Initially, as the temperature increases, the growth of In_2O_3 crystallites is retarded, and then, at temperatures above 450−500 °C, there is a sharp increase in the crystallite size, as compared with that for the individual In_2O_3 samples. This effect is more pronounced for the composites containing the higher content of TiO_2 (Figure 1).

3.2. TG/DSC Studies. Typical TG and DSC curves for xerogels of the pure oxides as well as $TiO_2-In_2O_3$ composites dried at 70 °C are presented in Figures 2 and 3.

In the case of pure oxides, the TG curves demonstrate a continuous weight loss up to 500 °C for TiO_2 and 600−650 °C for In_2O_3. Three main steps can be found. An initial weight loss from 70 to 160 °C for TiO_2 and to 200 °C for hydrous indium oxide is accompanied by an endothermic effect and can be related to the withdrawal of solvent residues and unbound stabilizing acid from the powders. A subsequent sharp decrease in the weight observed around 200−230 °C for hydrous indium oxide and at 160 °C for TiO_2 seems to be associated with removing the structural water. Theoretically, the removal of water molecules according to reaction $2In(OH)_3 = In_2O_3 + 3H_2O$ anticipates a weight loss of 16.3%, which is in good agreement with the experimental results (ca. 15%). This process is accompanied by a significant endothermic effect for the indium-containing xerogel and an exothermic effect for the TiO_2 powder (Figure 3). Above 240 °C, the weight loss becomes smoother and then is stopped.

A comparison of the TG and DSC curves obtained for the mixed hydrous oxide powders with those for pure oxides evidences that the process of dehydration of the composites is not a trivial superposition of the processes in the individual components and is markedly determined by their mutual influence (Figures 2 and 3). Therefore, the sharp weight loss accompanied by the exothermic effect is shifted to the region of higher temperatures as the content of hydrous indium oxide in the composite increases from 0 to 22 mol %, and for the $TiO_2(0.78)-In_2O_3(0.22)$ composite, this weight loss is observed even at 245 °C (Figure 2). The $TiO_2(0.54)-In_2O_3(0.46)$ composite demonstrates three steps of the sharp weight loss in the temperature range from 195 to 245 °C, with the exothermic effect being superimposed on the endothermic one (Figures 2 and 3)

Another peculiarity of the thermostimulated transformations in the composite systems is the appearance of a weight loss step in the high-temperature region (T > 500−550 °C) (Figure 2). This decrease in the weight ranges from 1% to 2% depending on the xerogel composition and is accompanied by a slight exothermic effect. The onset of this process falls well in the temperature range in which the retardation of the growth of In_2O_3 crystallites gives way to their accelerated growth (Figure

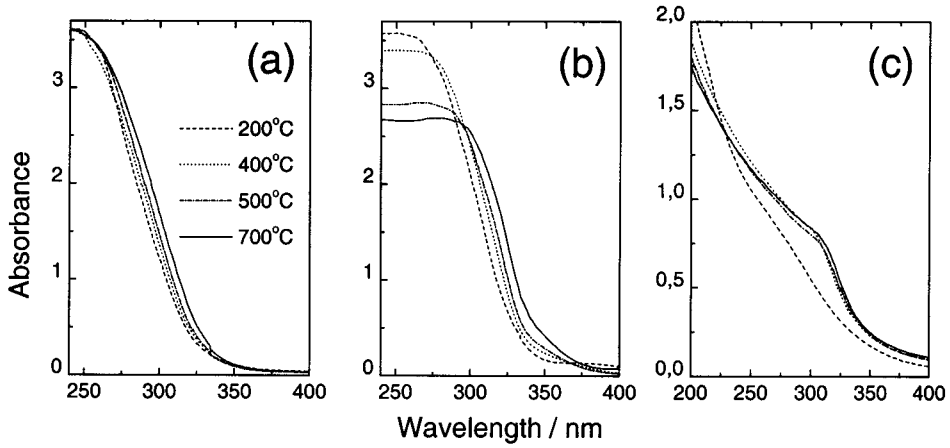

Figure 4. Absorption spectra of the $TiO_2(0.78)-In_2O_3(0.22)$ composite film (a) and single-component TiO_2 (b) and In_2O_3 (c) films annealed at different temperatures.

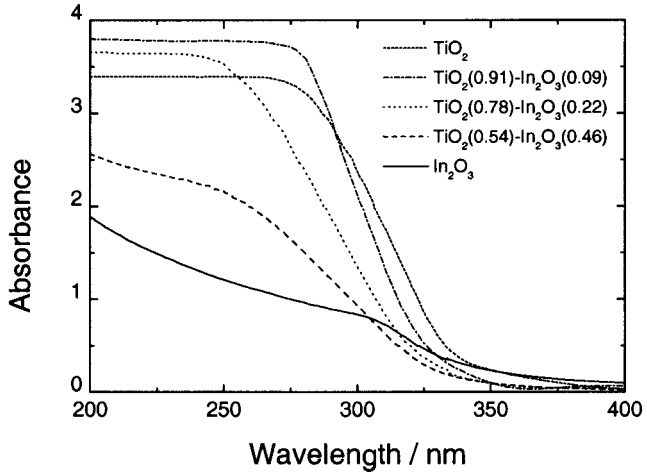

Figure 5. Absorption spectra of TiO_2 and In_2O_3 films and $TiO_2-In_2O_3$ composites annealed at 400 °C.

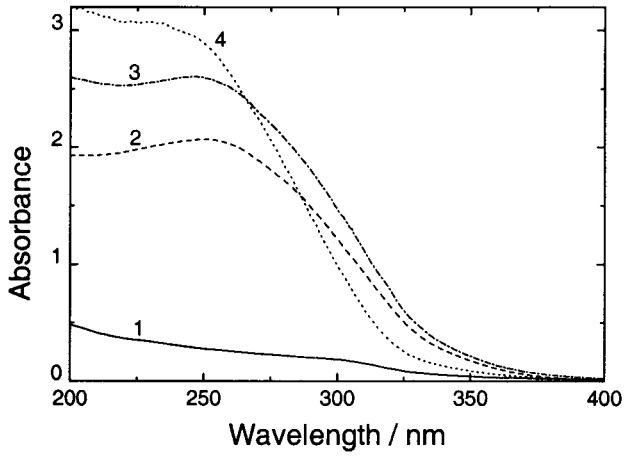

Figure 6. Absorption spectra of the $TiO_2(0.78)-In_2O_3(0.22)$ composite film (4), of individual TiO_2 (2) and In_2O_3 (1) films containing the same amounts of oxides which are present in the composite film, and of superimposed TiO_2 and In_2O_3 films (3).

1b). Taking into account this coincidence, we may infer that the acceleration of the In_2O_3 crystallite growth in the binary oxide systems is accompanied by the withdrawal of remains of structural water.

3.3. Optical Characteristics. Figure 4 shows UV−vis absorption spectra of the single-component (TiO_2 and In_2O_3) and $TiO_2(0.78)-In_2O_3(0.22)$ composite films heated at different temperatures. The sol−gel derived films obtained are characterized by a high transparency (transmittance more than 90%) in the visible region of the spectrum. As the annealing temperature increases, the UV absorption edges are shifted to lower energies (Figure 4). For the pure In_2O_3 films, this shift is the most distinct in the temperature range from 200 to 400 °C, and at $T > 400$ °C, it is negligible. It is in this temperature range that the basic part of the dehydration process is completed. For the pure TiO_2 films, the red shift of the absorption edge observed in the temperature interval from 500 to 700 °C can be associated with the anatase-to-rutile transformation. Characteristically, for composite films, this shift is smaller than that for the pure TiO_2 and In_2O_3 films.

Figure 5 presents absorption spectra of the films, annealed at 400 °C, with different Ti/In molar ratio. As the In_2O_3 content increases, the absorption edge moves toward the shorter wavelengths. To demonstrate that the absorption edge shift is not caused by merely optical effects associated, for example, with different magnitudes and spectral dependencies of absorbance for TiO_2 and In_2O_3, we have measured the absorption spectra of the $TiO_2(0.78)-In_2O_3(0.22)$ composite film and also those of the individual oxide films containing the same amounts of TiO_2 and In_2O_3 which are present in the composite film. These spectra together with the spectrum of the individual TiO_2 and In_2O_3 samples superimposed on one another are shown in Figure 6. A blue shift of the absorption edge of the composite film in reference to that of the individual TiO_2 film and of the superimposed samples is clearly evident from Figure 6. A possible explanation of this blue shift is presented in the next section.

Figure 7 shows refractive indexes (n) of the investigated films heated at 400 °C as a function of the film composition. The values of n change over a wide range from 1.64 for individual In_2O_3 to 2.3 for TiO_2 samples. Characteristically, the refractive index of the sol−gel derived TiO_2 films falls good in the range of values (2.2−2.5) reported for different anatase films,[16,30] whereas the n for nanocrystalline In_2O_3 samples is markedly lower than that (around 2.0) reported for compact In_2O_3 thin films.[31]

3.4. Photoelectrochemical Properties. Recently, considerable interest has been focused on studying coupled semiconductor particulate systems such as $CdS-TiO_2$,[32] $CdS-ZnO$,[33] TiO_2-WO_3,[7] TiO_2-SnO_2[34], and others. It has been revealed that such coupled semiconductor electrodes not only extend the photoresponse of large band gap semiconductors but also can improve the photocurrent generation.[7,32−34] In this connection,

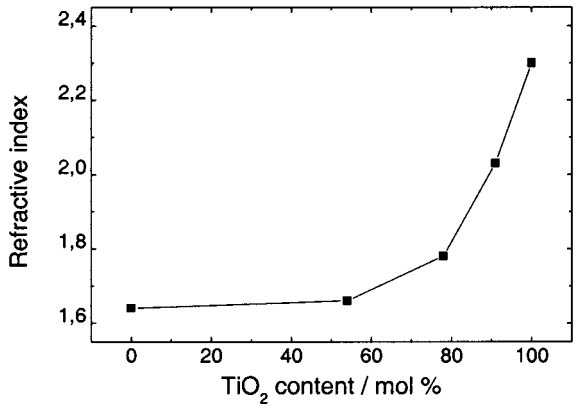

Figure 7. Refractive index measured at $\lambda = 500$ nm as a function of the film composition for $TiO_2-In_2O_3$ films annealed at 400 °C.

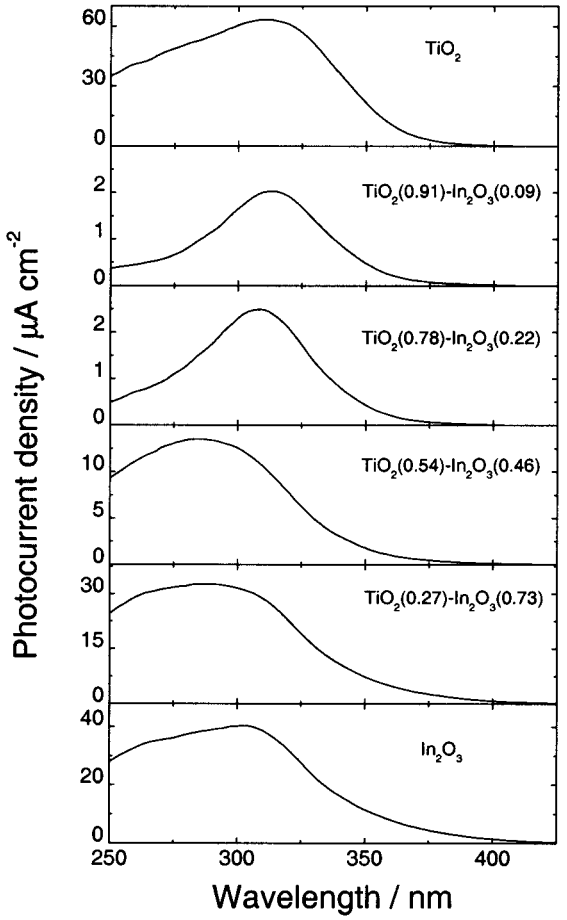

Figure 8. Photocurrent spectra of different $TiO_2-In_2O_3$ film electrodes annealed at 400 °C. Electrode potential: 0.5 V vs Ag|AgCl. Electrolyte: deaerated 0.1 M KOH solution containing 0.1 M CH_3COONa.

it has been of interest to investigate the photoelectrochemical properties of the $TiO_2-In_2O_3$ composite films prepared in the present work. In addition, the PEC method allowed us to obtain an important information on semiconductor characteristics of the systems under investigation.

The photocurrent spectra of the $TiO_2-In_2O_3$ composite film electrodes are compared with those of pure TiO_2 and In_2O_3 electrodes in Figure 8. All spectra were measured in an alkaline solution containing 0.1 mol/L CH_3COONa as a scavenger of photoholes. A marked decrease in the photocurrent for the binary oxide electrodes can be seen in comparison with single-component films. Characteristically, the photocurrent drop is more significant for the TiO_2-enriched composites than that for the In_2O_3-enriched ones. In addition, the TiO_2-enriched composite electrodes demonstrate the photocurrent spectra with the marked dip in the short-wavelength region of spectrum (Figure 8).

TABLE 1: Energies of Direct (E_{gd}) and Indirect (E_{gi}) Transitions Calculated from the Photocurrent Spectra for TiO_2 and In_2O_3 Films and $TiO_2-In_2O_3$ Composites

film composition (mol %)	E_{gd} (eV)	E_{gi} (eV)
TiO_2 (100%)	3.58	3.23
TiO_2 (91%)$-In_2O_3$ (9%)	3.65	3.28
TiO_2 (78%)$-In_2O_3$ (22%)	3.70	3.31
TiO_2 (54%)$-In_2O_3$ (46%)	3.77	3.07
TiO_2 (27%)$-In_2O_3$ (73%)	3.72	2.88
In_2O_3 (100%)	3.68	2.72

Using the photocurrent spectra shown in Figure 8, we determined the band gaps of the TiO_2 and In_2O_3 films and the efficient band gaps of the $TiO_2-In_2O_3$ composites annealed at 400 °C by plotting $(Y\hbar\omega)^n$ versus $\hbar\omega$ dependences, where Y is the quantum yield of photocurrent, $\hbar\omega$ is the photon energy, $n = 2$ for allowed direct, $n = {}^1/_2$ for allowed indirect, and $n = {}^1/_3$ for forbidden indirect optical transitions. Figure 9 shows these plots for the films with different composition. The E_{gd} and E_{gi} values obtained by extrapolating the linear portions of these plots are given in Table 1. A comparison of the $(Y\hbar\omega)^{1/2}$ versus $\hbar\omega$ and $(Y\hbar\omega)^{1/3}$ versus $\hbar\omega$ plots for the pure In_2O_3 films and In_2O_3-enriched composites shows that the better linearization and the wider linear portions are observed for the latter. This evidences that the indirect forbidden transitions are realized in these films in accord with the results of other researchers.[24,35] In this connection, the E_{gi} values for these samples have been obtained using $(Y\hbar\omega)^{1/3}$ versus $\hbar\omega$ plots (Figure 9c).

To compare the energetics of the conduction bands of TiO_2 and In_2O_3 particles studied, we have estimated the potential of the conduction band edge (the use of this term rather than "flat band potential" is preferable for nanostructured electrodes[36]) by measuring the photocurrent onset potential (E_{on}) of the electrodes. The photocurrent−potential curves for the TiO_2, In_2O_3, and $TiO_2-In_2O_3$ electrodes measured under polychromatic UV illumination are shown in Figure 10. The values of E_{on} are ca. −0.95 and −0.30 V for the pure TiO_2 and In_2O_3 films, respectively. Characteristically, the photocurrent onset potential for the $TiO_2(0.78)-In_2O_3(0.22)$ composite is even more negative (by ∼0.25−0.30 V) than that for the TiO_2 electrode. The results obtained evidence that the energetics of the conduction band edges of the TiO_2 and In_2O_3 particles favors the electron separation in the coupled $TiO_2-In_2O_3$ system. The conduction band electrons generated by UV light in the TiO_2 nanoparticles should transfer into the lower lying In_2O_3 conduction band, with reverse electron transfer being energetically forbidden. Moreover, if values of the direct band gaps of TiO_2 and In_2O_3 are taken into account, the position of valence band edges of these oxides should also favor the transfer of holes from In_2O_3 to TiO_2. In this connection, it is not clear why any increase in the quantum efficiency of photocurrent is not observed as a result of coupling TiO_2 and In_2O_3 particles by analogy with the previously studied nanoporous semiconductor coupled electrodes.[7,32−34] One of the causes of the above discrepancy may be the fact that recombination losses at the $TiO_2-In_2O_3$ interfaces mask the effect of increasing the photocurrent quantum yield due to coupling of the different semiconductor particles. In the composites studied, interface states can play an important role in the charge carrier transport owing to the extremely small size of the semiconductor particles.

Figure 11 presents the dependence of the maximum photocurrent on the film composition. To elucidate possible causes

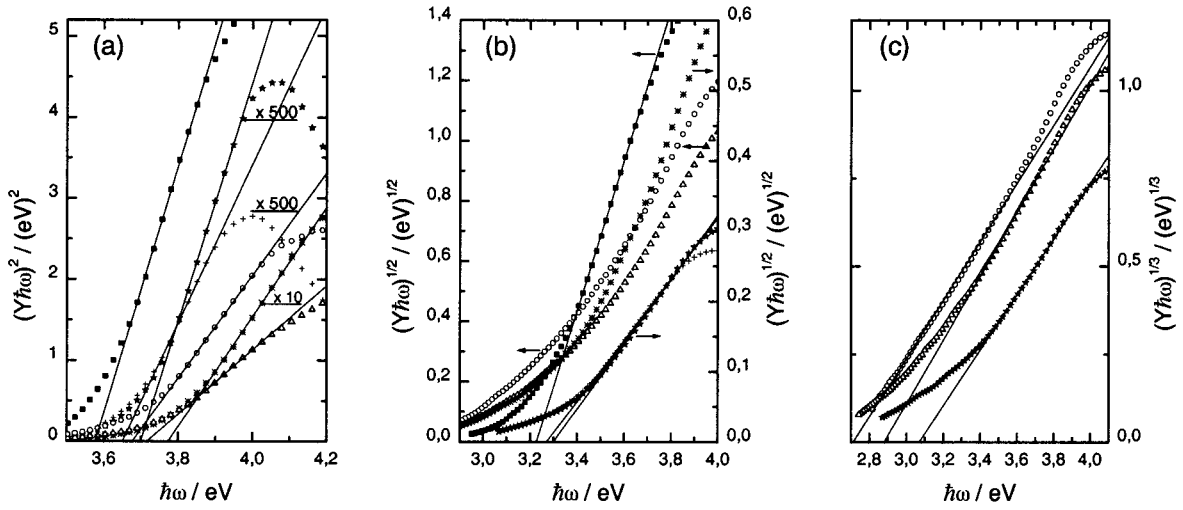

Figure 9. $(Y\ \hbar\omega)^2$ vs $\hbar\omega$ (a), $(Y\ \hbar\omega)^{1/2}$ vs $\hbar\omega$ (b), and $(Y\ \hbar\omega)^{1/3}$ vs $\hbar\omega$ (c) plots calculated from the photocurrent spectra of $TiO_2-In_2O_3$ film electrodes with the following composition: (■) TiO_2, (+) $TiO_2(0.91)-In_2O_3(0.09)$, (★) $TiO_2(0.78)-In_2O_3(0.22)$, (∗) $TiO_2(0.54)-In_2O_3(0.46)$, (△) $TiO_2(0.27)-In_2O_3(0.73)$, and (○) In_2O_3.

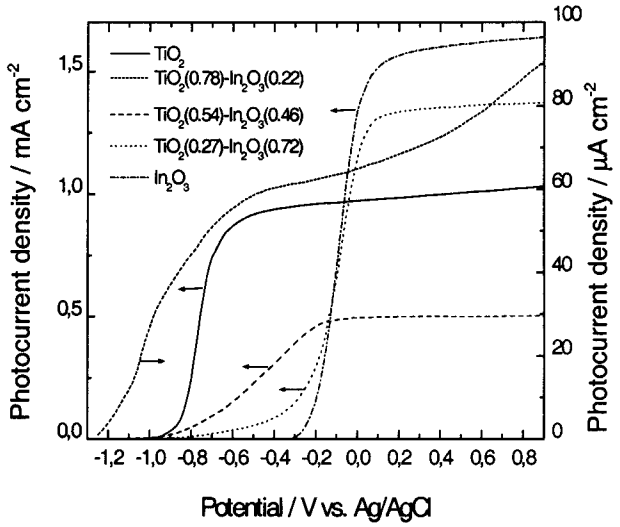

Figure 10. Photocurrent vs applied potential curves recorded under polychromatic UV illumination of different $TiO_2-In_2O_3$ film electrodes annealed at 400 °C. Electrolyte: deaerated 0.1 M KOH solution containing 0.1 M CH_3COONa. Potential sweep rate was 10 mV s^{-1}.

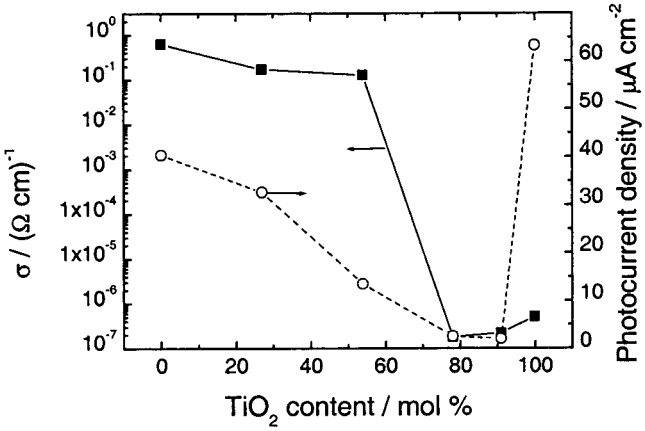

Figure 11. Electrical conductivity (■) and the maximum photocurrent (from photocurrent spectra) (○) of $TiO_2-In_2O_3$ films annealed at 400 °C as a function of the film composition.

of the marked decrease in photocurrent in going from the single-component electrodes to the $TiO_2-In_2O_3$ composites, we have measured the electric conductivity (σ) of the films under investigation. Figure 11 shows the conductivity of the samples annealed at 400 °C as a function of the film composition. The σ is low for the pure TiO_2 films and changes slightly with increasing the In_2O_3 content up to 22 mol %. Then the conductivity increases abruptly from 1.8×10^{-7} to 0.13 $(\Omega\ cm)^{-1}$ within the In_2O_3 concentration range from 22 to 46 mol % and alters slightly again at In_2O_3 content more than 46 mol %.

On the basis of the conductivity measurement data, we have inferred that the carrier transport in the $TiO_2-In_2O_3$ composites occurs mainly through In_2O_3 particles having significantly lower intrinsic resistivity. If so, the abrupt increase in the conductivity shown in Figure 11 may be related to the attainment of percolation threshold associated with the formation of 3D infinite clusters of interconnected In_2O_3 nanoparticles. Percolation phenomena have been studied in a number of real physical systems, for example, in cermets.[37] Therefore, Abeles et al. have revealed that the resistivity of nanoparticulate $W-Al_2O_3$ films increases abruptly in the vicinity of $x_c = 0.47$, where x_c is the volume fraction of the conducting phase (W).[37a] We have estimated the molar fraction of In_2O_3 in the $TiO_2-In_2O_3$ composites corresponding to the x_c of ca. 0.47. The calculated value (~32 mol %) falls well in the In_2O_3 content range within which the composite conductivity is sharply changed that evidences in favor of the above assumption.

To understand why the photocurrent decreases significantly in going from the single-component TiO_2 electrodes to the composites containing quite small amount of In_2O_3, we should consider the mechanism of photogenerated charge separation and transport in the nanostructured binary oxide system. In nanocrystalline nanoporous electrodes, in comparison with compact polycrystalline or single-crystal ones, the depletion layer is practically absent in semiconductor particles because of their small size.[36] Electrons and holes photogenerated in nanocrystallites are quickly trapped at the surface states, and furthermore, they can be independently involved in surface reduction and oxidation processes. Since nanostructured film has an extremely high specific area and the crystallites are surrounded by electrolyte over the whole film thickness, a key factor resulting in the decrease in photocurrent efficiency is the recombination of electron−hole pairs both directly via the surface states and via the PEC reaction products.[22,36] One of the ways of reducing the recombination losses is the quick

separation of photogenerated electrons and holes by possibly longer distances. Employing coupled semiconductor particles has been found to make possible such a separation and to increase markedly the photocurrent efficiency.[7,32a,34] The main reason for this efficient charge separation is the difference in relative energies of the conduction and valence bands of the interconnected semiconductors.

In order for the anodic photocurrent to flow in an electrode system, the photogenerated electrons must reach the substrate. In the case of binary oxide composites with the In_2O_3 content (>32 mol %) providing the percolation cluster formation, photoelectrons are readily transferred across In_2O_3 grain boundaries which are in direct contact with each other. In the case of TiO_2-enriched composites in which the percolation threshold cannot be reached, the photoelectrons trapped within In_2O_3 nanocrystallites cannot cross the $TiO_2-In_2O_3$ interface and reach the substrate. As a consequence, negligibly small photocurrents are observed for these composite electrodes (Figures 8 and 11). Similar effect has been observed by Bedja and Kamat for the TiO_2-capped SnO_2 nanocrystalline electrodes where the electrons trapped within SnO_2 nanoparticles were not be able to cross the TiO_2 shell and to reach a substrate.[34] It should be noted that the electrons photogenerated in TiO_2 nanocrystallites can be captured by In_2O_3 particles all the way to the substrate. The probability of this process should grow as the distance from the substrate increases. This seems to be responsible for the photocurrent dip observed in the short-wavelength region of the action spectra of TiO_2-enriched electrodes, since the light from this spectral range is absorbed mainly in the uppermost layers of the film.

Comparison of band gaps of pure TiO_2 and In_2O_3 with the efficient band gaps of the $TiO_2-In_2O_3$ composites shows that both E_{gd} and E_{gi} values have extreme dependencies on the film composition with maxima observed for binary oxide films containing 22−46 mol % of In_2O_3 (see Table 1). The enhanced band gaps and the blue-shifted absorption edges for the $TiO_2-In_2O_3$ composites as compared with the single-component films cannot be explained by the Burstein−Moss effect since the binary oxide films show no increase in conductivity in the TiO_2 concentration range from 100 to 78 mol % (Figure 11).

A blue shift of the absorption edge has been previously observed also in TiO_2-SiO_2 composites and assigned by a number of researchers to the quantum size effect in TiO_2 nanoparticles.[2−4] It should be noted that the manifestation of size quantization in titania particles is controversial, at least at the particle radius ≥1 nm. In a few recent works, a blue shift of the absorption edge has been revealed for sols and films containing very small TiO_2 particles in the size range from 1.0 to 12.0 nm and associated with Q-sized effects.[38] On the other hand, Serpone et al. have studied in detail anatase sols with particles sizes ranging from 2.1 to 26.7 nm and found no evidence for the band edge shift and hence quantum size effects.[39] These discrepant data, together with the absence of solid estimates of effective masses of charge carriers in TiO_2 and the weaknesses of effective mass model,[40] make any conclusions on size quantization in titania rather premature. However, the possibility of manifestation of Q-sized effects should not be completely ruled out in the case of the $TiO_2-In_2O_3$ composites involving very small semiconductor particles.

Another possible explanation of the blue-shifted band edges for $TiO_2-In_2O_3$ samples may be a marked influence of different surface and interface species on the optical spectra. These might be coordinatively unsaturated surface species (e.g., TiO_x with $x < 6$), surface species with dangling bonds (e.g., $HO-Ti-(OTi)_5$ or $H_2O-Ti-(OTi)_5$), and Ti−O−In cross-linking bonds. For composites involving nanosized crystallites of the metal oxides, the concentration of such species might be noticeable. The presence of tetrahedral coordinative titanium ions and Ti−O−Si or Ti−O−Al cross-linking bonds has been previously revealed for titanium dioxide supported on Vycor glass[41] and silica[42] or dispersed into SiO_2[4] and Al_2O_3 matrixes.[43] As shown in those works, the presence of such species induces the large blue shift of the band edge. Luca et al. have revealed five-coordinate Ti sites on anatase surfaces in nanostructured TiO_2 xerogels by EXAFS and XANES methods and discussed their strong influence on the optical absorption spectra.[44] Although we have no direct evidences of the presence of the above-mentioned species in the $TiO_2-In_2O_3$ composites, their existence can be indirectly confirmed by the occurrence of structural water in the binary oxide samples which is withdrawn only at high temperatures more than 500 °C.

4. Conclusions

In the present work, we have studied the crystalline structure, thermostimulated transformations, and optical and photoelectrochemical properties of $TiO_2-In_2O_3$ mixed films and xerogels prepared via the sol−gel technique using stabilized hydrous titanium dioxide and indium hydroxide sols. The samples have a nanocrystalline structure, with the crystallite size depending on the sample composition and on the annealing temperature. There is a strong mutual influence of the components of the binary oxide system during its thermal treatment which manifests itself in TG and DSC measurements and in a marked suppression of the TiO_2 crystallite growth in the composites. However, no evidence for indium titanate formation has been found in the composite system, at least in the temperature range investigated.

Optical and PEC spectroscopy measurements have shown that the band gap edge of the composite films is blue-shifted, as compared with that of single-component films. The energy of direct and indirect transitions passes through a maximum as the In_2O_3 content increases. The enhanced efficient band gaps of the composites have been assigned to a combination of possible quantum size effects and interface phenomena.

From the conductivity and photoelectrochemical measurements, it follows that the charge transport in the $TiO_2-In_2O_3$ composite films is mainly through interconnected In_2O_3 particles and drastically facilitates when 3D infinite cluster of them forms. Efficient separation of photogenerated charge carriers occurs in the interconnected TiO_2 and In_2O_3 particles, owing to the favorable energetics of the conduction bands of these oxides.

Acknowledgment. We are grateful to Dr. L. S. Ivashkevich and Dr. A. S. Lyahov for assistance with XRD measurements.

References and Notes

(1) Dislich, H. In *Sol-Gel Technology for Thin Films, Fibers, Preforms, Electronics and Specialty Shapes*; Klein, L. C., Ed.; Noyes: Park Ridge, NJ, 1988; p 50.
(2) Davis, R. J.; Liu, Z. *Chem. Mater.* **1997**, *9*, 2311.
(3) Liu, Z.; Davis, R. J. *J. Phys. Chem.* **1994**, *98*, 1253.
(4) Anpo, M.; Nakaya, H.; Kodama, S.; Kubokawa, Y.; Domen, K.; Onishi, T. *J. Phys. Chem.* **1986**, *90*, 1633.
(5) Benesi, H. A.; Winquist, B. H. C. *Adv. Catal.* **1978**, *27*, 97.
(6) Gottsche, J.; Hinsch, H.; Wittwer, V. *Sol. Energy Mater. Sol. Cells* **1993**, *31*, 415.
(7) Shiyanovskaya, I.; Hepel, M. *J. Electrochem. Soc.* **1999**, *146*, 243.
(8) Camino, D.; Deroo, D.; Salardenne, J.; Treuil, N. *Sol. Energy Mater. Sol. Cells* **1995**, *39*, 349.
(9) Wu, Y.; Hu, L.; Jiang, Z.; Ke, Q. *J. Electrochem. Soc.* **1997**, *144*, 1728.

(10) Gurlo, A.; Bârsan, N.; Ivanovskaya, M.; Weimar, U.; Göpel, W. *Sens. Actuators, B* **1998**, *47*, 92.
(11) Anderson, W. B. *Paint Varnish Prod.* **1953**, *43*, 33.
(12) Lusvardi, V. S.; Pierce, K. G.; Barteau, M. A. *J. Vac. Sci. Technol., A* **1997**, *15*, 1586.
(13) Hoffmann, M. R.; Martin, S. T.; Choi, W.; Bahnemann, D. W. *Chem. Rev.* **1995**, *95*, 69.
(14) Linsebigler, A. L.; Lu, G.; Yates, J. T., Jr. *Chem. Rev.* **1995**, *95*, 735.
(15) O'Regan, B.; Grätzel, M. *Nature* **1991**, *353*, 737.
(16) Hovel, H. J. *J. Electrochem. Soc.* **1978**, *125*, 983.
(17) Hamberg, I.; Granqvist, C. G. *J. Appl. Phys.* **1986**, *60*, R123.
(18) Jarzebski, Z. M. *Phys. Status Solidi A* **1982**, *71*, 13.
(19) Yamaura, H.; Tamaki, J.; Moriya, K.; Miura N.; Yamazoe, N. *J. Electrochem. Soc.* **1996**, *143*, L36.
(20) Gurlo, A.; Ivanovskaya, M.; Pfau, A.; Weimar U.; Göpel, W. *Thin Solid Films* **1997**, *307*, 288.
(21) O'Regan, B.; Moser, J.; Anderson, M.; Grätzel, M. *J. Phys. Chem.* **1990**, *94*, 8720.
(22) Poznyak, S. K.; Kokorin, A. I.; Kulak, A. I. *J. Electroanal. Chem.* **1998**, *442*, 99.
(23) Tahar, R. B. H.; Ban, T.; Ohya, Y.; Takahashi, Y. *J. Appl. Phys.* **1997**, *82*, 865.
(24) Poznyak, S. K.; Kulak, A. I. *Electrochim. Acta* **2000**, *45*, 1595.
(25) Uhlmann, D. R.; Motakef, S.; Suratwala, T.; Young, J.; Boulton, J. M.; Zelinski, J. J.; Gardlung, Z.; Teowee, G.; Cronin, *J. Proc. SPIE* **1994**, *2*, 2288.
(26) In *Handbook of Nanostructured Materials and Nanotechnology*; Nalwa H. S., Ed.; Academic Press: New York, 2000.
(27) Abeles, F. *C. R. Acad. Sci., Paris* **1949**, *228*, 553.
(28) Rozdin, I. A.; Spiridonov, F. M.; Komissarova, L. N.; Plyuschev V. E. *Neorg. Mater.* **1971**, *7*, 1798.
(29) Milligan, W. *J. Phys. Colloid Chem.* **1951**, *55*, 497.
(30) (a) Fitzgibbons, E. T.; Sladek, K. J.; Hartwig, W. H. *J. Electrochem. Soc.* **1972**, *119*, 735. (b) Blackwood, D. J.; Greef, R.; Peter, L. M. *Electrochim. Acta* **1989**, *34*, 875. (c) Ohtsuka, T.; Nomura, N. *Corros. Sci.* **1997**, *39*, 1253. (d) Hass, G. *Vacuum* **1952**, *2*, 331.
(31) (a) Müller, H. K. *Phys. Status Solidi* **1968**, *27*, 723. (b) Szczyrbowski, J.; Dietrich, A.; Hoffmann, H. *Phys. Status Solidi (a)*, **1982**, *69*, 217. (c) Nagatomo, T.; Maruta, Y.; Omoto, O. *Thin Solid Films* **1990**, *192*, 17. (d) Gerfin, T.; Grätzel, M. *J. Appl. Phys.* **1996**, *79*, 1722.
(32) (a) Vogel, R.; Pohl, K.; Weller, H. *Chem. Phys. Lett.* **1990**, *174*, 241. (b) Gerischer, H.; Luebke, M. *J. Electroanal. Chem. Interfacial Electrochem.* **1986,** *204*, 225.
(33) Hotchandani, S.; Kamat, P. V. *J. Phys. Chem.* **1992**, *96*, 6834.
(34) Bedja, I.; Kamat, P. V. *J. Phys. Chem.* **1995**, *99*, 9182.
(35) (a) Weiher, R. L.; Ley, R. P. *J. Appl. Phys.* **1966**, *37*, 299. (b) Raza, A.; Agnihotri, O. P.; Gupta, B. K. *J. Phys. D: Appl. Phys.* **1977**, *10*, 1871.
(36) Hagfeldt, A.; Gratzel, M. *Chem. Rev.* **1995**, *95*, 49.
(37) (a) Abeles, B.; Pinch, H. L.; Gittleman, J. I. *Phys. Rev. Lett.* **1975**, *35*, 247. (b) Pinch, H. L. *J. Vac. Sci. Technol.* **1974**, *12*, 60.
(38) (a) Kormann, C.; Bahnemann, D. W.; Hoffmann, M. R. *J. Phys. Chem.* **1988**, *92*, 5196. (b) Kavan, L.; Stoto, T.; Grätzel, M.; Fitzmaurice, D.; Shklover, V. *J. Phys. Chem.* **1993**, *97*, 9493. (c) Anpo, M.; Shima, T.; Kodama, S.; Kubokawa, Y. *J. Phys. Chem.* **1987**, *91*, 4305. (d) Choi, W.; Termin, A.; Hoffmann, M. R. *J. Phys. Chem.* **1994**, *98*, 13669.
(39) Serpone, N.; Lawless, D.; Khairutdinov, R. *J. Phys. Chem.* **1995**, *99*, 16646.
(40) Rama Krishna, M. V.; Friesner, R. A. *J. Chem. Phys.* **1992**, *96*, 8309.
(41) Anpo, M.; Aikawa, N.; Kubokawa, Y.; Che, M.; Luis, C.; Giamello, E. *J. Phys. Chem.* **1985**, *89*, 5017.
(42) Lassaletta, G.; Fernandez, A.; Espinos, J. P.; Gonzalez-Elipe, A. R. *J. Phys. Chem.* **1995**, *99*, 1484.
(43) Anpo, M.; Kawamura, T.; Kodama, S.; Maruya, K.; Onishi, T. *J. Phys. Chem.* **1988**, *92*, 438.
(44) Luca, V.; Djajanti, S.; Howe, R. F. *J. Phys. Chem. B* **1998**, *102*, 10650.